Petroleum Science 22 (2025) 2312–2324

Contents lists available at ScienceDirect

Petroleum Science

journal homepage: www.keaipublishing.com/en/journals/petroleum-science

Original Paper

# Study on an improved saturation parameter method based on joint inversion of NMR and resistivity data in porous media

Peng-Ji Zhang [a], Bao-Zhi Pan [a], Yu-Hang Guo [a, *], Li-Hua Zhang [a], Zhao-Wei Si [b], Feng Xu [b], Ming-Yue Zhu [a], Yan Li [a]

[a] *State Key Laboratory of Deep Earth Exploration and Imaging, College of Geoexploration Science and Technology, Jilin University, Changchun, 130026, Jilin, China*

[b] *Exploration and Development Research Institute, Jidong Oilfield Company, PetroChina, Tangshan, 063000, Hebei, China*

ARTICLE INFO

*Article history:*
Received 20 October 2024
Received in revised form
16 November 2024
Accepted 20 March 2025
Available online 21 March 2025

Edited by Meng-Jiao Zhou

*Keywords:*
NMR $T_2$ spectrum
Fluid distribution
Tight sandstone
Groundwater saturation
Three–pore segment saturation model
Rock pore structure

ABSTRACT

$CO_2$ storage capacity is significantly influenced by the saturation levels of reservoir rocks, with underground fluid saturation typically evaluated using resistivity data. The conductive pathways of fluids in various states within rock pores differ, alongside variations in conductive mechanisms. To clarify the conductivity of water in rocks across different states, this study employed a three–pore segment saturation model, which corrected for the additional conductivity of clay by categorizing water into large–pore segment, medium–pore segment, and small–pore segment types. Addressing the heterogeneity of tight sandstone reservoirs, we classified distinct pore structures and inverted Archie equation parameters from NMR logging data using a segmented characterization approach, yielding dynamic Archie parameters that vary with depth. Ultimately, we established an improved saturation parameter method based on joint inversion of NMR and resistivity data, which was validated through laboratory experiments and practical downhole applications. The results indicate that this saturation parameter inversion method has been effectively applied in both settings. Furthermore, we discussed the varying conductive behaviors of fluids in large and medium pore segment under saturated and drained states. Lastly, we proposed a workflow for inverting saturation based on downhole data, providing a robust foundation for $CO_2$ storage and predicting underground fluid saturation.

## 1. Introduction

The flow field within porous media, such as rocks, serves as the space and channels for storing and transporting oil, gas, and water. Factors influencing the properties of porous media and fluid flow include pore structure, pore fluid characteristics, and their interactions (Qiu et al., 2020; Xu et al., 2023). Groundwater, a vital component of these resources, plays a key role in supporting the Earth's ecosystem (Viaroli et al., 2022; Haggerty et al., 2023). Water saturation is the most critical parameter for evaluating the flow of pore fluids within rocks. In oil and gas exploration, the accuracy of water saturation calculations directly reflects current oil recovery levels and the extent of oilfield development (Heidary, 2021; Guo et al., 2022). In hydraulic engineering, geotechnical engineering, and mining, cracks and pores in rocks provide reservoir space for free water (Wasantha et al., 2018; Zhang and Gao, 2015). In practical engineering applications, the mechanical properties of rocks under varying water saturation states, along with the conductive mechanisms of water in these rocks, can also be investigated (Ming et al., 2020; Bai et al., 2022; Xu et al., 2024). Rock porosity is a critical parameter influencing the physical and mechanical properties of rocks and the migration behavior of subsurface fluids, making its study highly significant in fields such as hydraulic engineering, geotechnical engineering, and mining. For instance, in hydraulic engineering, rock porosity directly affects groundwater seepage characteristics and the stability of dam foundations; in geotechnical engineering, it serves as a key indicator for evaluating foundation bearing capacity and rock mass stability; and in mining, porosity is closely related to ore deposit conditions and resource extraction efficiency (Zhao et al., 2022; Kyeongmo and Hyunki, 2023). However, current research on the variation patterns and influencing factors of porosity under complex rock conditions remains insufficient. This study adopts innovative experimental and modeling approaches to

---

* Corresponding author.
*E-mail address:* guoyuhang@jlu.edu.cn (Y.-H. Guo).

https://doi.org/10.1016/j.petsci.2025.03.024

focus on the conductivity laws of porous media, further exploring the relationships between pore distribution, fluid flow behavior within pore spaces, and electrical conductivity. The findings aim to provide scientific evidence and theoretical support for addressing related engineering challenges. Furthermore, water saturation plays a significant role in $CO_2$ geological storage technology. Estimating the final storage capacity of carbon dioxide in aquifer solutions, as well as understanding the migration and distribution of injected $CO_2$ in geological structures, relies on evaluating water saturation in underground rock pore spaces (Bachu and Adams, 2003; Jongwon and Hu, 2016; Zhang et al., 2018; Abidoye and Das, 2020). Based on geological conditions, storage prerequisites, storage significance, and the stability of $CO_2$ storage, a target area for $CO_2$ geological storage should be selected to ensure superior reservoir conditions, appropriate burial depth, proximity to $CO_2$ capture facilities, and a suitable elevation (Wang et al., 2023). Additionally, the heterogeneity of the reservoir must be considered when exploring the residual trapping mechanisms (Luo et al., 2022).

Methods for calculating water saturation can be categorized into four types. The first type is the classical Archie equation, which is applicable to clean formations (Archie, 1942). The second type includes saturation models that account for shale content, such as the Simandoux equation (Simandoux, 1963), W–S model (Waxman and Smits, 1968), Indonesia saturation equation (Poupon and Leveaux, 1971), dual water model (Clavier et al., 1984), and three–water model (Mo et al., 2001). These models assess saturation based on the relationship between reservoir fluid saturation and resistivity derived from conventional logging curves. The third type calculates saturation using NMR logging data or establishes relationships between parameters based on a combination of conventional logging curves and NMR logging data (Coates et al., 1999; Heidary, 2021; Ge et al., 2023). In the fourth type, water saturation is determined through deep learning methods (Barros and Andrade, 2013; Zhong et al., 2021; Kim et al., 2022).

The segmented evolution (or segmented analysis) method has demonstrated powerful analytical capabilities in analyzing the pore structures of porous media. By subdividing the pore space, it improves the precision of understanding complex pore structures. Fractal dimension, as an indicator of pore structure complexity, has been successfully applied to evaluate the permeability and storage capacity of porous media. However, further exploration is needed to effectively integrate fractal dimension and segmented analysis methods into practical engineering applications (Katz and Thompson, 1985; Duan et al., 2023; Liu et al., 2024; Huang et al., 2024). NMR logging technology is highly sensitive to fluid properties and pore structure information, unaffected by electrical and lithological properties. It provides extensive insights into fluids, pore structure, and even rock wettability (Jackson, 1984; Korb, 2018; Michael et al., 2022). In wells, conversion models applied to NMR logging data allow the derivation of rock physical parameters not accessible through conventional logging instruments (Guo et al., 2016, 2022; Liu et al., 2016), representing a novel approach. Regarding saturation modeling, some scholars propose a power function relationship between $T_2$ and the resistivity index ($I$) within specific saturation ranges, yet have not explored model parameters in detail. Multiple linear regression models are employed alongside formulas like the Archie equation to establish correlations between $T_2$ and $I$, facilitating saturation calculations (Feng et al., 2020a, 2020b). Theoretical models are developed to relate NMR $T_2$ values with resistivity indexes, enabling the calculation of water saturation using various saturation indexes (Xiao et al., 2021). While these methods can calculate water saturation by linking NMR $T_2$ spectrum and resistivity, their accuracy may diminish in rocks with pronounced heterogeneity and complex pore structures. This study utilizes NMR logging data to employ a rock physics parameter conversion model and segmented characterization method, extracting dynamic Archie parameters and assessing saturation (Pan et al., 2018; Guo et al., 2022). This combined approach considers the pore structure of igneous rocks, yielding depth–variable saturation parameters through segmented characterization. However, the saturation calculation model does not incorporate variations in lithology coefficient $a$ or cementation index $m$ with depth.

In this study, petrophysical experiments were conducted on rock samples obtained, and the internal pore structure of the rock was classified. Due to the complex pore structure and strong heterogeneity of rocks, fluid distribution within rock pores varies, leading to different conductivity behaviors. By integrating the Archie formula with fractal theory, we enhanced the parameter–solving approach of the three–pore segment saturation model. Combining NMR logging data with fractal theory allowed us to derive depth–dependent cementation exponent $m$ and lithology coefficient $a$. We introduced the equivalent pure rock resistivity increase index $I^*$ to eliminate the additional conductivity of clay. This index extended the original relationship between NMR transverse relaxation time and $I^*$. Using a segmented characterization method, we inverted coefficients $b$ and saturation index $n^*$ from NMR logging data. Furthermore, we explored the distribution of fluids in different pore spaces and investigated the relationship between fractal dimension and electrical properties of pore space. From the perspectives of conduction mechanisms, pore size distribution, and fluid allocation, we discussed the correlation between transverse relaxation time and conductivity in porous media. The improved saturation parameter method, based on joint inversion of NMR and resistivity data, established in this study, provides robust technical support for groundwater saturation calculation and evaluation of $CO_2$ storage capacity.

## 2. Characterization of pore structure

### 2.1. Relationship between physical parameters

In the laboratory, permeability and porosity were measured using an AP608 Automated Permeameter–Porosimeter from Core–Test Co. The porosity of the 15 sandstone samples ranged 5.21%–11.89%, while permeability ranged 0.13–1.41 mD. The samples exhibited a strong pore–permeability relationship (Fig. 1(a)), characteristic of typical tight sandstone with low porosity and permeability. The overall relationship between rock sample permeability ($K$) and quality factor ($RQI$) $RQI = \sqrt{\frac{K}{\varphi}}$ was good (Fig. 1(b)). XRD analysis revealed that the reservoir minerals in the study area were primarily quartz, with an average clay content exceeding 20%, predominantly consisting of illite (Fig. 1(c) and (d)).

### 2.2. Characterization of pore structure

Underground rock samples were collected and subjected to various petrophysical experiments, including assessments of physical properties, electrical properties, capillary pressure curves, and NMR $T_2$ spectra (Fig. 2). The experimental data were analyzed to attribute electrical differences among the rock samples to a combined effect of physical properties and pore structure. The instrument used in this experiment was the IME–MRI–D2 high–performance low–field nuclear magnetic resonance microanalysis system. The experimental measurement frequency was 2 MHz, the echo interval was 200 μs, the waiting time was 3 s, the number of echoes was 4096, and the number of scans was 64. The maximum centrifugal frequency was 8000 rpm. For the measurement of the capillary pressure curve, the mercury intrusion method was employed using the AutoPore IV 9505 pore structure analyzer.

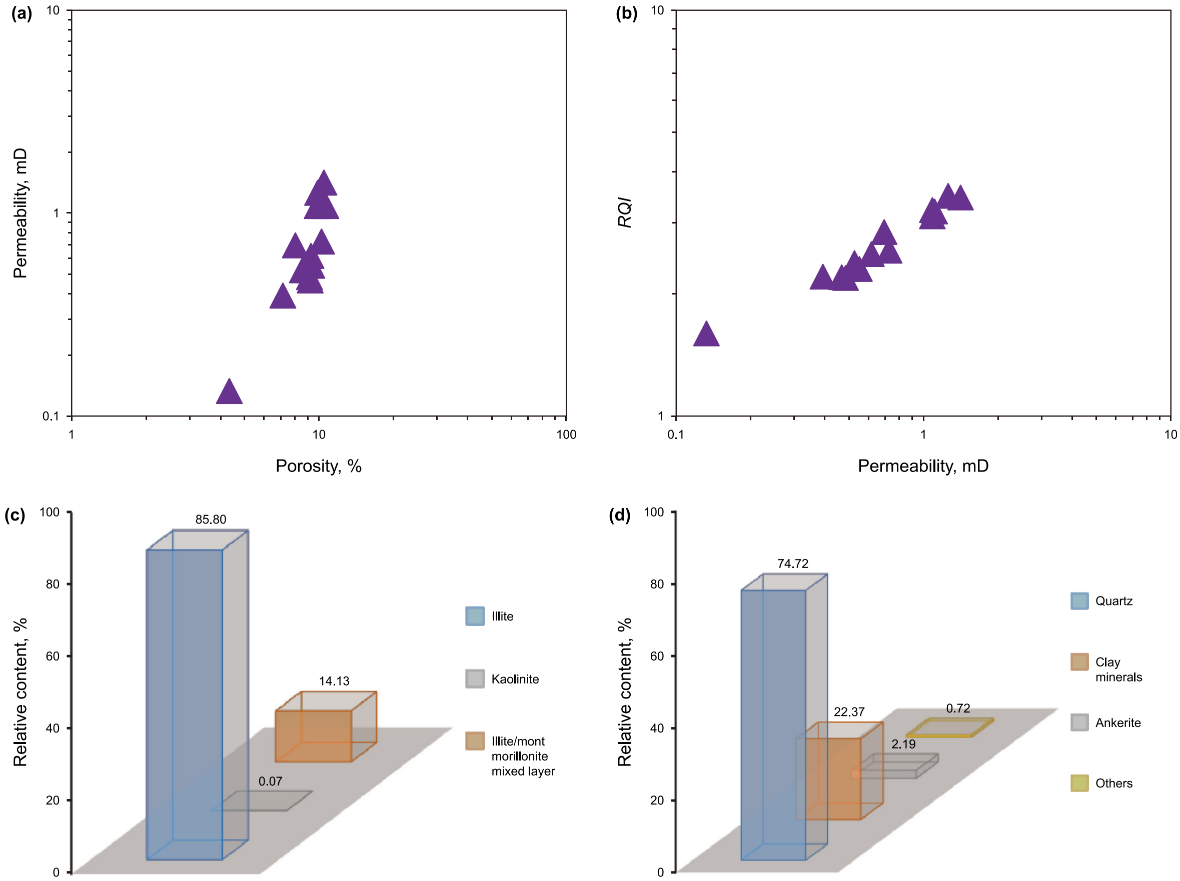

**Fig. 1.** Some petrophysical results of rock samples **(a)** porosity and permeability; **(b)** intersection of permeability and *RQI*; **(c)** XRD experimental analysis results; **(d)** clay mineral analysis.

Given the complexity and diversity of pore structures in the samples, three distinct pore types were categorized, and their characteristic parameters were determined separately (Table 1). In the mercury intrusion capillary pressure (MICP) curve, where *SHg* is the saturation of mercury, pore radius of 0.02 μm and 1 μm can indeed be regarded as "inflection points" for pore structure and water saturation. Studies have shown that pores smaller than 0.02 μm contribute almost nothing to permeability, primarily because the fluid flow resistance in these tiny pores is significant, making it difficult to form effective seepage paths (Fig. 2(a) and (b)). Meanwhile, at a pore radius of 1 μm, the incremental mercury intrusion reaches its maximum, indicating that the pore throat structure at this size has the most significant impact on fluid saturation. Therefore, setting 0.02 μm as the boundary between small–pore segment and medium–pore segment, and 1 μm as the boundary between medium–pore segment and large–pore segment, is reasonable and consistent with experimental observations. This classification method effectively reflects the impact of pore structure on permeability and fluid distribution, providing a basis for pore classification and seepage characteristic studies in rocks. However, high resonance frequencies caused rapid NMR signal decay, limiting the collection of complete reservoir relaxation information. Typically, reservoir fluid NMR signals were excited in a uniform field at a resonance frequency of 2 MHz (Anand and Ali, 2015; Byeungju et al., 2019). Previous studies have recommended using magnetic field environments as close as possible to downhole conditions when calibrating NMR logging interpretation parameters through core experiments. In this study, increasing magnetic field intensity generally shifted the $T_2$ spectra of samples toward shorter relaxation times, resulting in a decrease in the geometric mean of $T_2$ (Qin et al., 2021; Liu et al., 2023). The NMR experiments conducted $T_2$ spectrum measurements of rock samples at a frequency of 2 MHz, which closely resembles actual downhole conditions but may not fully capture the distribution of small–pore segment. Therefore, the focus of this study primarily centers on converting the $T_2$ spectral distribution of medium–pore segment and large–pore segment.

## 3. Theory and method

### 3.1. The three–pore segment saturation model

The new three–water model proposes that in formations containing formation water, free pore water, microcapillary pore water, and clay water, each component conducts electricity in parallel (Fig. 3), with their conductivities following the Archie equation. The model's separate treatment of clay water adheres to objective principles and provides a comprehensive insight into the conductive mechanisms of rocks (Zhang et al., 2010).

In the study area, the average absolute clay content in rock samples is approximately 23%, indicating well–developed small–pore segment and high bound water saturation. Previous research and theoretical analyses suggest that clay bound water predominantly occupies small–pore segment, microcapillary water is found in mesopores, and free water exists in macropores (Cheng et al., 2024; Song et al., 2024). The main problem of the three-water model is that it fails to fully consider the complexity of the pore structure and its significant effect on electrical conductivity and

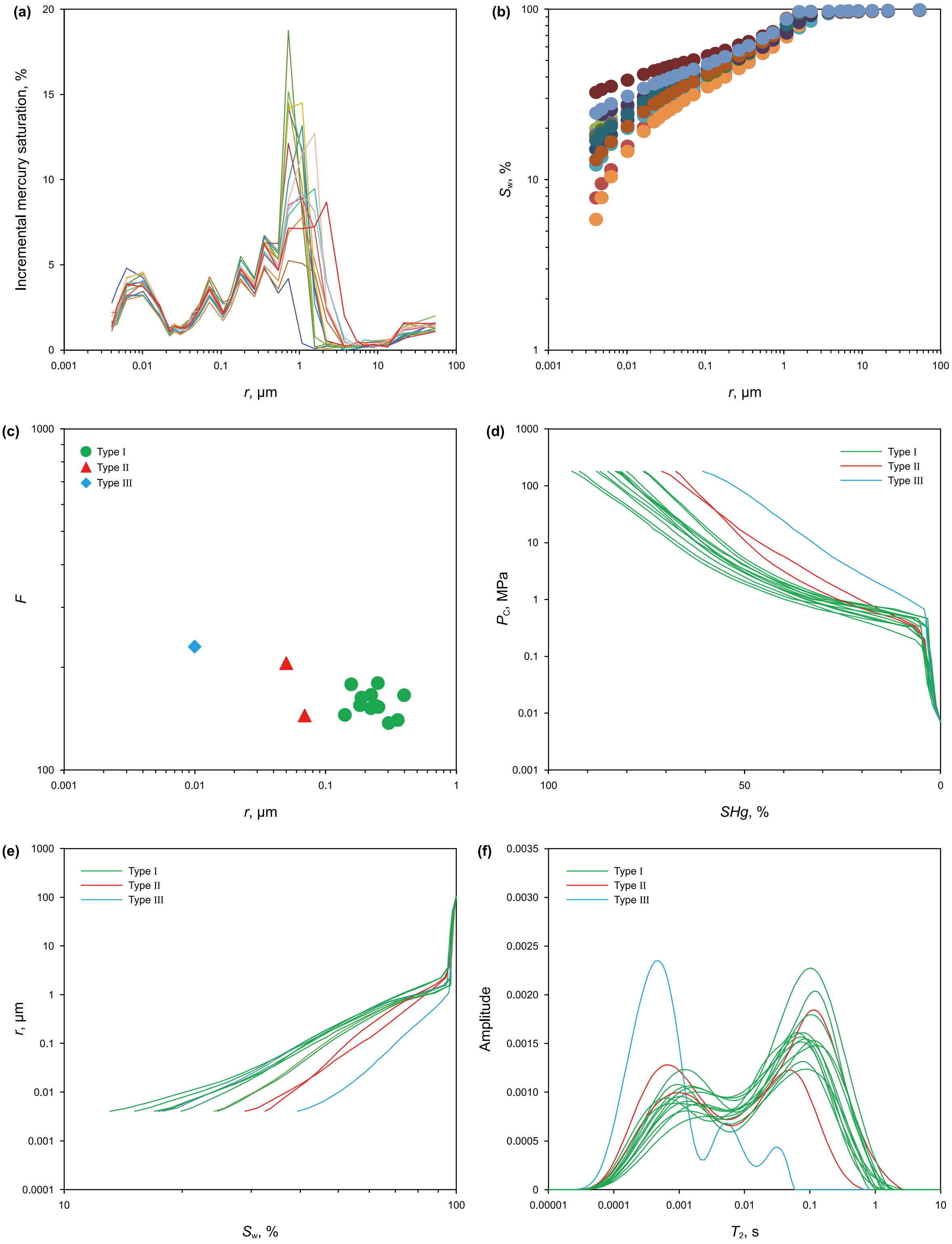

**Fig. 2.** Classification of pore structure of rock samples **(a)** throat radius and incremental mercury saturation; **(b)** pore throat radius and water saturation; **(c)** median pore throat radius and formation factors; **(d)** classified mercury intrusion experimental curves; **(e)** classification saturation versus pore throat radius intersection plot; **(f)** classified nuclear magnetic resonance $T_2$ spectrum curve.

mobility. Firstly, the three-water model is unable to distinguish the differences between small, medium and large pore segment in terms of storage capacity and permeability performance, especially in the transition region between microcapillary water and free water, and the model is too simple to describe the changes in mobility. Secondly, the three-water model ignores the important role of pore-throat connectivity on the seepage path and conductive network, which makes it difficult to accurately reflect the

**Table 1**
Various characteristic parameters of the rock samples.

| Pore structure type | Average porosity, % | Average permeability, mD | Maximum mercury saturation, % | Radius mean, μm | Average pore throat radius, μm | Average median pore throat radius, μm |
|---|---|---|---|---|---|---|
| I | 10.126 | 0.762 | 83.928 | 0.553 | 0.700 | 0.243 |
| II | 8.090 | 0.394 | 71.132 | 0.376 | 0.656 | 0.050 |
| III | 5.210 | 0.133 | 60.717 | 0.132 | 0.265 | 0.010 |

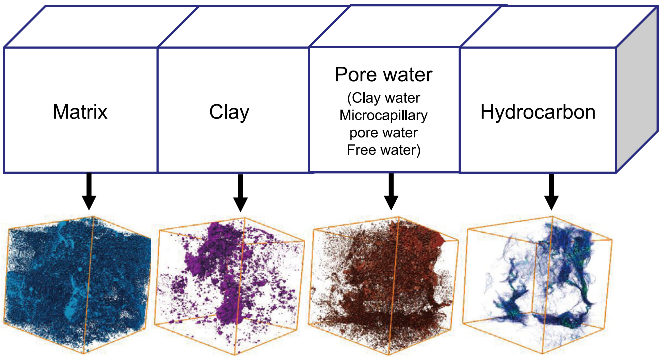

**Fig. 3.** Schematic diagram of the new three–water saturation model.

influence of pore distribution on the conductive properties of the reservoir. These shortcomings limit the application of the three-water model in fine reservoir characterisation and model construction.

In order to quantitatively describe the saturation distribution characteristics of the fluid within the three-pore segment, a three-pore segment saturation model is established in this paper.

The rock resistivity response equation becomes the following:

$$C_0 = \frac{1}{R_0} = \frac{\varphi_L^{m_L}}{a_L R_w} + \frac{\varphi_M^{m_M}}{a_M R_w} + \frac{\varphi_S^{m_S}}{a_S R_{swc}} \tag{1}$$

where $C_0$ is the electrical conductivity of the formation when it is 100% water, S/m; $R_0$ is the rock resistivity at 100% water saturation; $\varphi_L$, $\varphi_M$ and $\varphi_S$ are the porosity of large–pore segment, medium–pore segment, small–pore segment, respectively; $m_L$, $m_M$ and $m_S$ are the cementation exponent of large–pore segment, medium–pore segment, small–pore segment, respectively; $a_L$, $a_M$ and $a_S$ are the lithology coefficient of large–pore segment, medium–pore segment, small–pore segment, respectively.

Capillary water and clay water in small–pore segment are generally in a bound state, while microcapillary water can only flow under specific conditions, such as during drainage (Pan et al., 2018; Guo et al., 2022). Consequently, when hydrocarbons are present within the reservoir, the free fluid is replaced by hydrocarbons, resulting in a two–phase flow process within the large–pore segment. Using the Archie equation, we can derive the following:

$$C_t = \frac{1}{R_t} = \frac{S_{Lwf}^{n_L} \varphi_L^{m_L}}{a_L R_w} + \frac{\varphi_M^{m_M}}{a_M R_w} + \frac{\varphi_S^{m_S}}{a_S R_{swc}} \tag{2}$$

where $C_t$ is the electrical conductivity of the rock, S/m; $R_t$ is the electrical resistivity of the rock, Ω·m; $S_{Lwf}$ is the water saturation in large–pore segment; and $n_L$ is the corresponding saturation index.

### 3.2. Improved $T_2$–$I^*$ model

NMR experiments are capable of characterizing pore size distribution and evaluating pore structure. Previous studies have identified a power function relationship between transverse relaxation time and saturation index at specific wetting phase saturations. Following petrophysical experiments, it was determined that all rock samples in the study area exhibit water–wet characteristics. The relationship between the $T_2$–$I$ model and fractal dimension can be understood through fractal theory and the multi–scale properties of the medium. The pore structure of porous media or rocks is typically complex and exhibits self–similarity, with fractal theory providing an effective tool to describe such structures. The fractal dimension, as a quantitative indicator of pore complexity, significantly influences electrical transport properties such as conductivity and resistivity. In fractal structures, the scale and morphology of pores affect the flow paths of electrical current and the distribution of charge, thereby determining the material's conductivity. Therefore, changes in the fractal dimension not only affect the relaxation characteristics of water molecules in the $T_2$ spectrum but also influence the resistivity increase coefficient ($I$) by modifying the electrical response of the pores. For porous media, employing the three–pore segment saturation model, Archie's formula, and fractal theory, we delve into the conduction mechanism. By integrating pore size distribution in porous media, we expand on the fractal dimension across different pore spaces. This approach establishes the relationship between transverse relaxation time and resistivity index, elucidating the calculation of parameters $a$ and $m$ (based on petrophysical experimental data, obtain the porosity of small–pore segment, medium–pore segment, and large–pore segment, and substitute these values into Eqs. (A.16)–(A.19) in the appendix to calculate the parameters $a$ and $m$ corresponding to each pore segment. The calculation method exposes distinct microstructural characteristics within the porous medium and provides a framework for assessing the conductivity of different pore waters in relation to rock. Detailed derivations are provided in the Appendix. Based on the three–pore segment saturation model, we can obtain an equivalent pure rock resistivity index $I^*$:

$$I^* = \frac{C_{0sd}}{C_{tsd}} = \frac{C_0 - C_{0cl}}{C_t - C_{tcl}} = \frac{C_0 - C_{0cl}}{C_t - C_{0cl}} = \frac{b}{S_w^{n^*}} \tag{3}$$

where $C_{0cl}$ denotes the conductivity due to the additional electrical conductivity of the clay in the small–pore segment, S/m; $C_{tcl}$ denotes the conductivity due to the additional electrical conductivity of the clay in the small-pore segment of the hydrocarbon-bearing rocks, S/m; $C_{0sd}$ is the conductivity of water-saturated pure sandstone, S/m; $C_{tsd}$ is the conductivity of partially water–saturated pure sandstone, S/m; $n^*$ is the equivalent pure rock saturation index. In practice, $C_{0cl}$ and $C_{tcl}$ can be regarded as equal, fully reflecting the dominant role of small–pore segments in the additional electrical conductivity of clay.

By substituting the equivalent pure rock resistivity index $I^*$ established in the $T_2$–$I$ model (Guo et al., 2018, 2022), the following can be obtained:

$$T_{2D} = b_t (I^*)^{-\alpha} \tag{4}$$

$$\alpha = \frac{n_t}{n^* \left(3 - D_{fT}\right)} \tag{5}$$

$$b_t = b^{\frac{n_t}{n^* \left(3 - D_{fT}\right)}} \tag{6}$$

where $T_{2D} = T_2/T_{2max}$, $T_{2max}$ is the $T_2$ maximum lateral relaxation time and $T_{2D}$ is the diffusion relaxation time; $\alpha$ is an exponent related to the pore radius distribution and relaxation time; $b_t$ is the conversion coefficient; $n_t$ is empirical coefficients; $D_{fT}$ is the fractal dimension that can be calculated using NMR data. Eqs. (4)–(6) is the improved $T_2$–$I^*$ model in this paper.

The parameters $b$ and $n$ that vary with depth can be obtained by Eq. (4), and the dynamic parameters $a$ and $m$ can be obtained by combining Archie equation and fractal dimension theory, which provides a theoretical basis for calculating saturation (Archie, 1942; Wei et al., 2015).

## 4. Results

The relationship between the geometric mean of $T_2$ ($T_{2lm}$) and the throat radius ($r$) as established experimentally, yielding the correlation shown in Fig. 4(a). Based on these relationships, medium–pore segment, medium–pore segment, and small–pore segment were classified, and the parameters $a$ and $m$ in the three–pore segment saturation model were determined using Eqs. (A.16)–(A.19) in the Appendix. and the parameters $b$ and $n^*$ were determined using Eqs. (3) and (4).

Laboratory comparisons of different saturation models demonstrated that the water saturation calculated using the three–pore segment saturation model effectively describes the electrical characteristics of tight sandstone (Fig. 4(g) and (h)). The calculated $n$ value aligned well with the measured value (with small–pore segment parameters obtained through optimization algorithms). Therefore, water saturation can be computed with the three–pore segment saturation model using these improved parameters. On the pore size scale, variations in the $\alpha$ values (as defined in Eq. (4)) were observed across different pore size ranges. Through segmented conversion, the actual and calculated $\alpha$ values exhibited good agreement (Fig. 4(b)), confirming that capillary pressure data and NMR $T_2$ distribution can be inferred from resistivity data. Notably, the $I^*$–$S_w$ curve fitted from the NMR data conversion showed strong consistency with the $n^*$ (Fig. 4(c)–(e)). Fig. 4(d) and (f) provide a detailed explanation of the $T_2$ spectrum calculated using the $T_2$–$I^*$ model based on the $I^*$–$S_w$ curve data. It can be seen from Fig. 4(d) and (f) that the segmented NMR $T_2$ distribution also conformed well morphologically, and the position and distribution of the main peak showed obvious high consistency.

In the description of the experimental results, we compared the relationship between the laboratory measurements and the calculated values, finding a high degree of consistency in both trends and numerical results. However, due to the strong heterogeneity, complex pore structures, and high clay content of these rock samples, certain commonly used conductivity models exhibited some deviations in their calculations. This further demonstrates the accuracy and applicability of the three–pore segment saturation model and the $T_2$–$I^*$ model established in this study for evaluating the conductivity of complex porous media.

## 5. Application of the model

The study area, the Ordos Basin, is known for its irregular distribution of sand bodies and pronounced heterogeneity. The varied distribution of fluids in rock pores significantly impacts rock conductivity. To enhance the accuracy of water saturation calculations and further facilitate the application of $CO_2$ storage technology in tight sandstone reservoirs, this study introduces an improved saturation parameter method based on the joint inversion of NMR and resistivity data (Fig. 5). This method is structured into the following six steps.

Step 1: Conduct analysis of experimental data and classify pore structures. Through analysis of core rock physical experiment data, pore structures were classified.

Step 2: Analyze and discuss fluid flow characteristics within rock pores, and establish the theoretical model. Considering the rock characteristics of low porosity and low permeability reservoirs with well–developed small–pore segment in tight sandstone, the occurrence states and conductive mechanisms of the three types of water were analyzed and discussed (according to petrophysical experiments such as mercury intrusion and nuclear magnetic resonance). Subsequently, a three–pore segment saturation model was formulated to compute water saturation.

Step 3: Establish a method for determining parameters in the three–pore segment saturation model. By integrating the Archie equation and fractal theory, we refined the parameter calculation $m$ and lithology coefficient $a$ (Appendix Eqs. (A.16)–(A.19)) were derived using NMR logging. In this way, the parameters $a$ and $m$ that vary with depth can also be obtained in the well, which can better evaluate the saturation.

Step 4: Expand and establish the $T_2$–$I^*$ model to derive dynamic evaluation parameters. Utilizing the three–pore segment saturation model, we introduced an equivalent pure rock resistivity index $I^*$ was established to eliminate the influence of additional conductivity of clay. The coefficient $b$ and $n^*$ in NMR logging data were inverted using a segmented characterization method (Eqs. (3)–(6)).

Step 5: Validate with laboratory data and models. Validate the method established for determining parameters in the three–pore segment saturation model using experimental data. Compare the calculated $C_0$ with laboratory measurements to assess the model's application effectiveness in laboratory settings. Demonstrate the applicability of the extended $T_2$–$I^*$ model through forward and inverse modeling of NMR $T_2$ spectrum distributions and rock electrical curves. If NMR logging data is unavailable, optimization algorithms can be employed to determine parameters and calculate water saturation.

Step 6: Conduct field application and evaluate the effectiveness. Introduce the dynamic parameters $a$, $b$, $m$, and $n^*$ established in the laboratory into the downhole application (mainly applied in calculating water saturation using Archie's formula). Then, compare the water saturation calculated using the dynamic and static parameters developed in this study with industry airflow test data to assess the effectiveness of the methods.

Fig. 6 is a comprehensive logging interpretation of the Ordos Basin, China using the $T_2$–$I^*$ model. The calculated water saturation results can be compared with industrial test results to evaluate the reservoir. The seventh is the water saturation calculated using the three–pore segment saturation model. The eighth is the calculation results of water saturation based on joint inversion of NMR and resistivity data. Due to the inability of downhole NMR logging to fully display the information of small–pore segment, in this study an improved Simandoux saturation equation was adopted to calculate the additional conductivity of the clay (Wang et al., 2016), while the conductivity of the large and medium pore segment water was calculated using a three–pore segment saturation model parameter calculation method. The twelfth is the industrial airflow

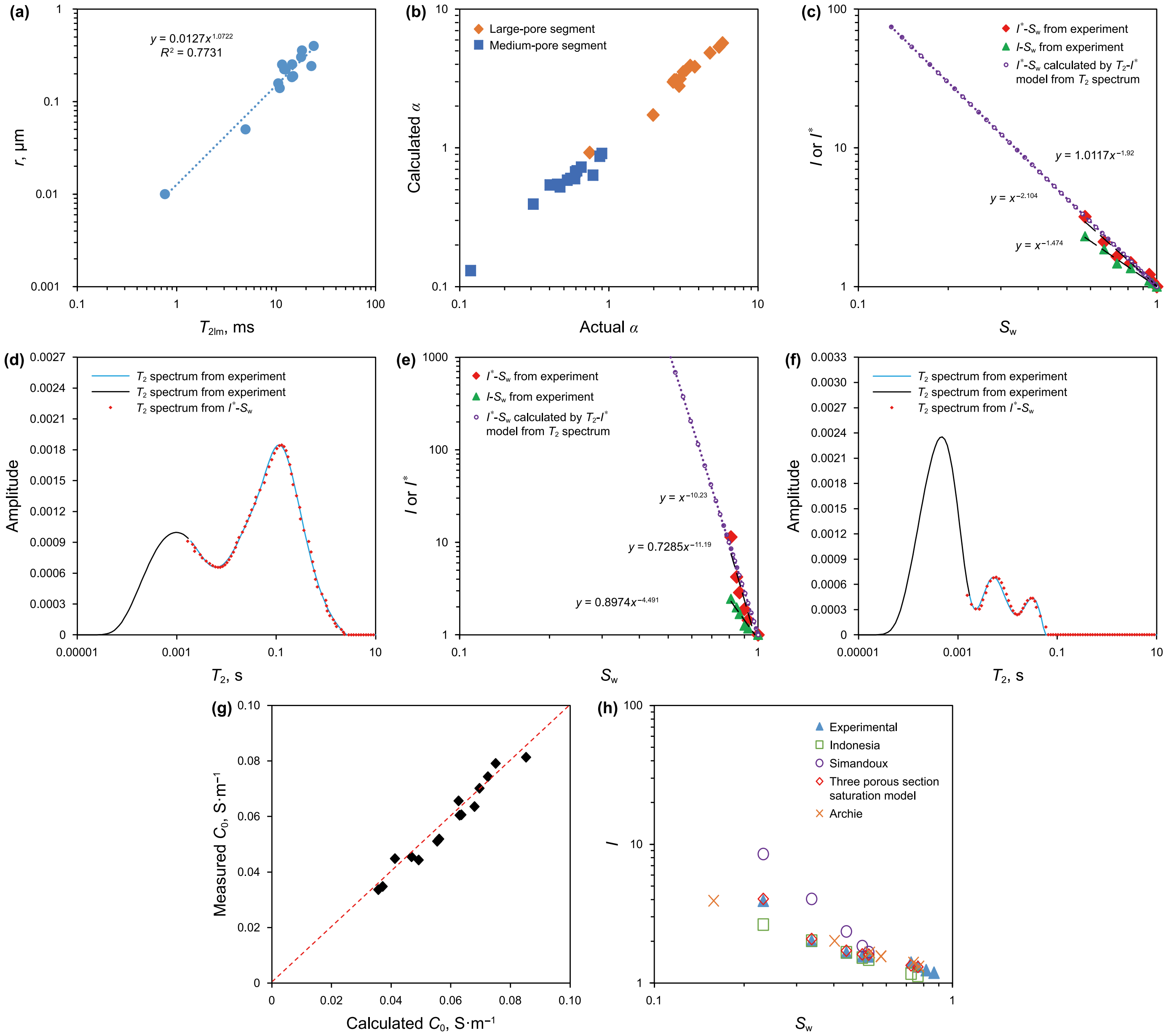

**Fig. 4.** The transformation results of $T_2$ and I or $I^*$ for cores. **(a)** and **(c)** show $I^*$–$S_w$ data calculated by $T_2$–$I^*$ model from $T_2$ spectrum; **(b)** and **(d)** show $T_2$ spectrum calculated by $T_2$–$I^*$ model from $I^*$–$S_w$ data; **(e)** comparison of calculated water saturation with different saturation models; **(f)** comparison of actual and calculated $\alpha$; **(g)** $C_0$ comparison; **(h)** comparison of different model $I$–$S_w$ relationships.

test data. The test results show that the daily production of gas in this layer was 14,724 m$^3$. According to industrial standards, this layer is considered a gas bearing formation. Based on the comparison of the results of the seventh and eighth calculations, the water saturation calculated by the dynamic parameters suggests a gas bearing formation and can better reflect the vertical heterogeneity of the reservoir, which is more in line with the actual situation. Therefore, based on the experimental results of this study, it is believed that the proposed $T_2$–$I^*$ model is quite effective in calculating the water saturation of tight sandstone reservoirs.

## 6. Discussion and possible implications

The fractal dimension reflects the degree of microscopic heterogeneity of the pore structure of the reservoir through the pore frequency. The fractal dimension of the pore size of the porous media is directly related to the conductivity, $D_{fT}/\varphi$ (The fractal dimension of large or medium pore segment is obtained from the mercury intrusion data/$\varphi$) can be used to characterise the distribution of the pore size under the current porosity of the porous media. The more the distribution of pore size in the rock, the more developed the pore structure of large and medium pore segment, which provides a better conductive path for the fluid, the enhanced conductivity, and the smaller the saturation index $n^*$ value becomes (Fig. 7).

Following the drainable experiments, the reduced area of the microcapillary water pore peak was quite large, indicating strong connectivity of the microcapillary water pore peak (Fig. 8(a)). For the same rock sample, as the water saturation decreased, the $T_2$ geometric mean ($T_{2lm}$) showed a gradually decreasing trend, and when reaching the irreducible water saturation, the $T_{2lm}$ reached its minimum (Fig. 8(b)).

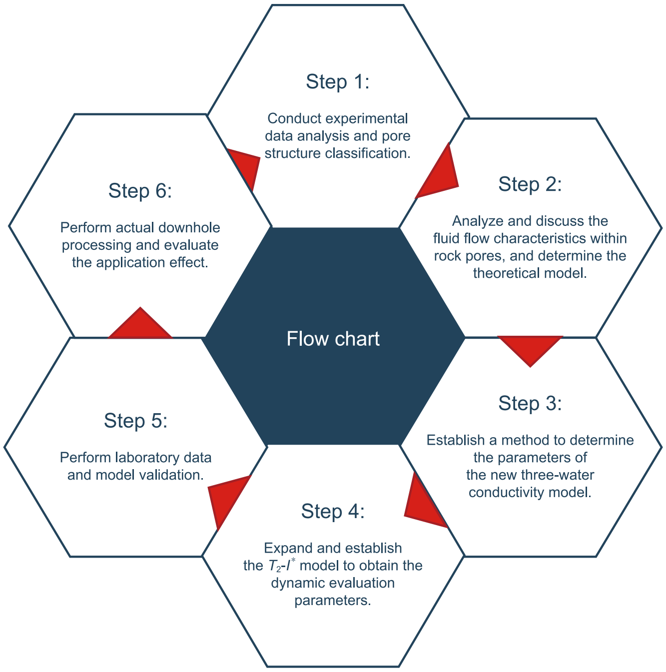

**Fig. 5.** Downhole practical application flow chart.

By comparing the fractal dimensions of large and medium pore segment at different saturation levels. In the large–pore segment, as the water saturation increased, the fractal dimension of the pore space gradually decreased, indicating that the fluid distribution in the large–pore segment conformed to Darcy's law (Fig. 8(c)). In the medium–pore segment, as the water saturation increased, the fractal dimension of the pore space changed irregularly (Fig. 8(d). The phenomenon of restricted diffusion in medium–pore segment relative to large–pore segment led to changes in the relaxation time of medium–pore segment, consequently resulting in irregular changes in the fractal dimension of medium–pore segment (Guo et al., 2016; Xie et al., 2023; Song et al., 2024). From the analysis of fluid distribution in the pore space, it is found that the tight sandstone in the study area has a complex pore structure and strong heterogeneity. The distribution of fluid in the pores is altered by drainable force, which together leads to changes in the distribution of fluid in the pores.

$D_{fT}$ is the use of NMR data to calculate the fractal dimension of the fluid in the pore space, $T_{2lm}$ can be used to characterise the distribution characteristics of the pore space. $T_{2lm}$ is also affected by the $n^*$, and the $n^*$ is a parameter related to the relaxation time, indicating that the fluid distribution in the pore space of porous media is directly related to the conductivity. $n^*$ is considered a qualitative measure of the efficiency of the current that can occur in partially saturated rocks, with the higher the efficiency, the lower the saturation index (Han et al., 2021). According to the modeling scheme proposed by Michelle (Michelle et al., 2010), conductivity and its efficiency are inversely proportional to the increase in the path length occupied by the current around the surface of an ideal insulating particle dielectric. As $T_{2lm\text{-}L,M}$ (the geometric mean of pore space between large– and medium–pore segment water, as shown in Fig. 9(a)) increases, indicating more pore structures corresponding to the large and medium pore segments, the proportion of fluid in these segments also increases. Consequently, the conductivity contribution $H_{L,M}$ (the ratio of conductivity of large and medium–pore segment water to the conductivity of fully saturated water) also increases, enhancing the overall conductivity contribution (Fig. 9(a) and (b)).

When $H_{L,M}$ is close to 1 (only large and medium pore segments are filled with water), the fluid conductivity in these pore segments is the strongest, and the efficiency for current flow is the highest. Consequently, the saturation exponent $n^*$of the corresponding rock reaches its lowest value (Fig. 9(c)), which is consistent with the conclusion of Han (Han et al., 2021). It is clear from the above analysis that the $n^*$ varies with the $H_{L,M}$ of large and medium pore segment water (Fig. 9(c)). The $H_{L,M}$ ranged from 0.36 to 0.76, and the $n^*$ varied from 8.08 to 2.46, with a change of 5.62, which was large, and the relationship between the $H_{L,M}$ and the $n^*$ was closer to the power index. The $H_{L,M}$ of large and medium pore segment water ranged from 0.76 to 1, and the $n^*$ changed from 2.55 to 1.51, with a change of only 1.04, and the change trend was not obvious, and the relationship between the $H_{L,M}$ and the $n^*$ was more linear. This indicates that at low water saturation, the water in the

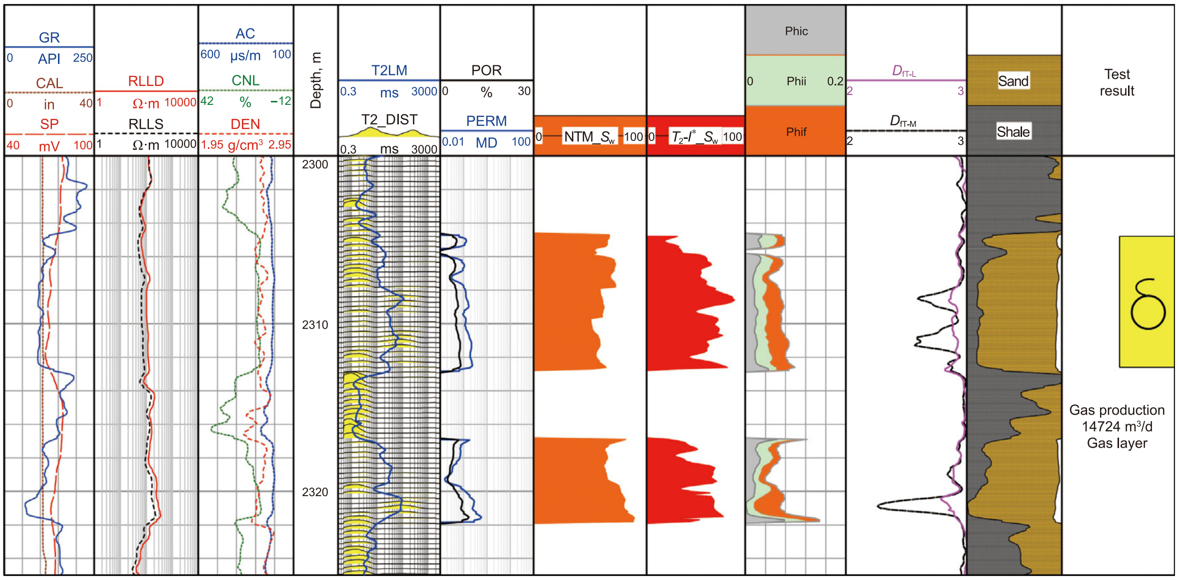

**Fig. 6.** Comprehensive logging interpretation of well A using the $T_2$–$I^*$ model in the Ordos Basin, China.

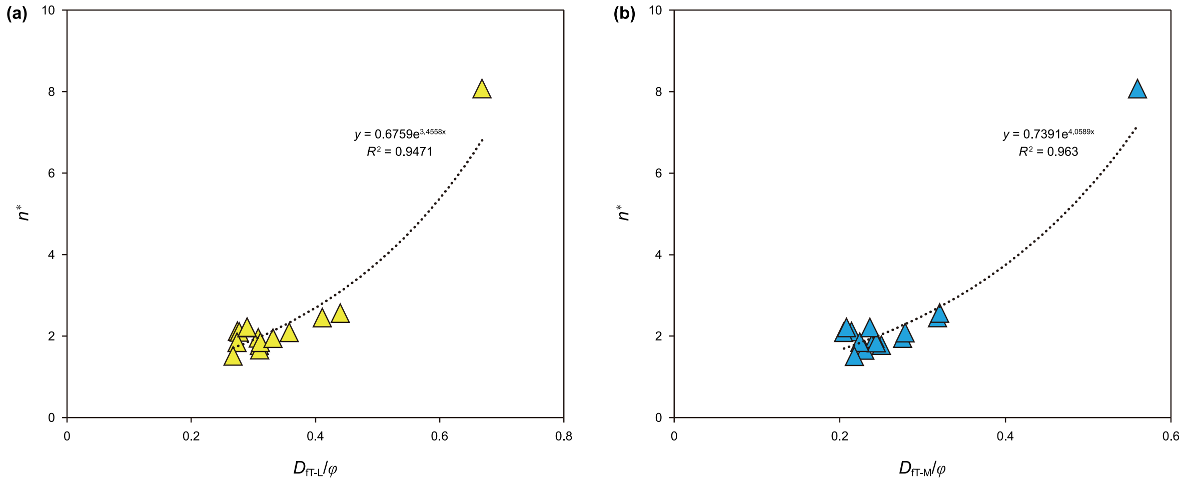

**Fig. 7.** Pore size distribution and conductivity of porous media: **(a)** intersection of $D_{\text{fT-L}}/\varphi$ (fractal dimension of large–pore segment) and saturation index $n^*$; **(b)** intersection of $D_{\text{fT-M}}/\varphi$ (fractal dimension of medium–pore segment) and $n^*$.

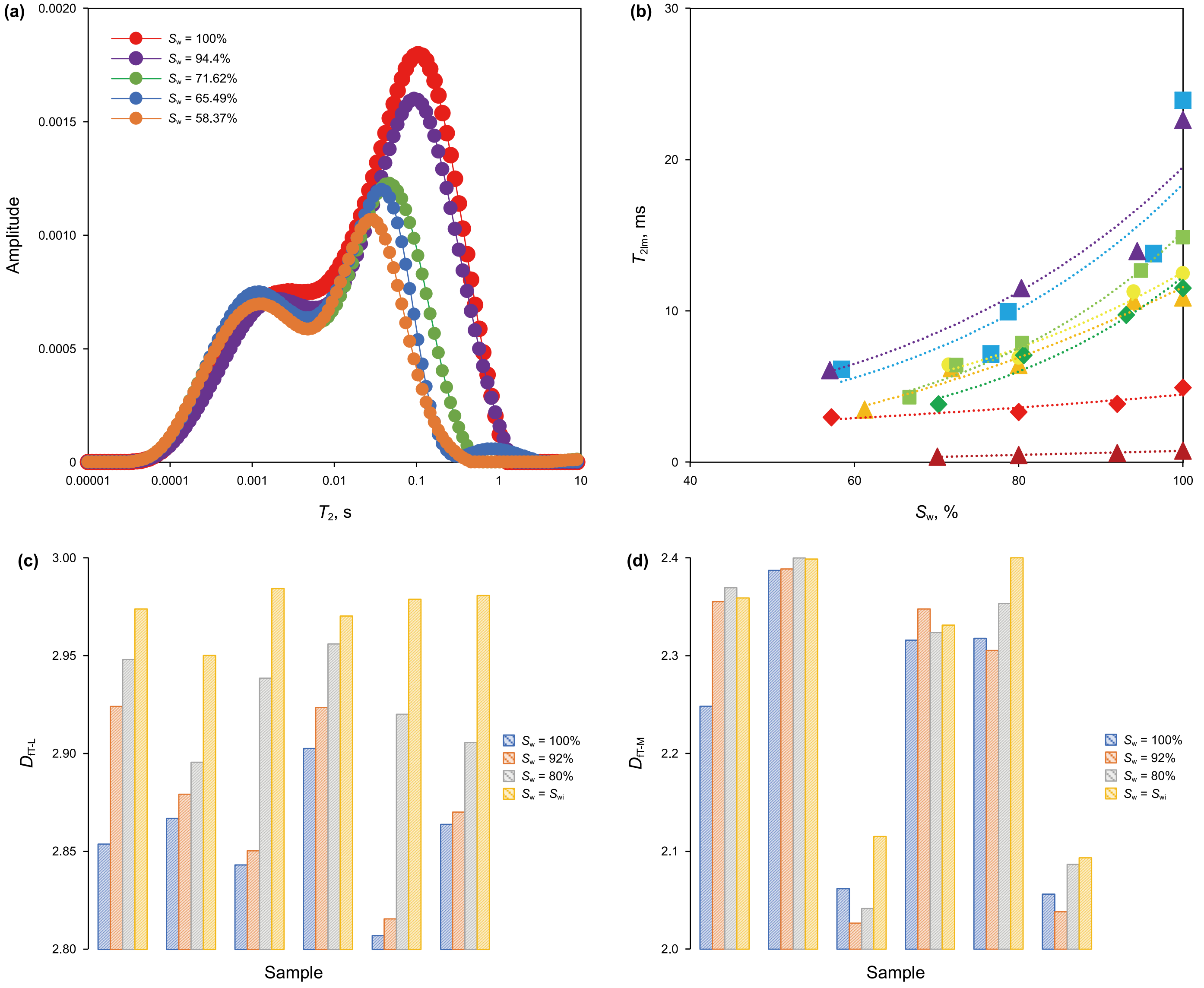

**Fig. 8.** Study on the distribution of fluid in porous media pore space: **(a)** NMR $T_2$ spectra at different saturations, **(b)** $S_w$–$T_{2\text{lm}}$ relationship for different rock samples, **(c)** $D_{\text{fT-L}}$ variation relationship for large–pore segment at different water saturations, **(d)** $D_{\text{fT-M}}$ variation relationship for medium–pore segments at different water saturations of rock samples.

small–pore segment conducts electricity and the $n^*$ is high, and with increasing water saturation, the water in the large and medium pore segment plays a decisive role in the conductivity. When $H_{\mathrm{L,M}}$ reaches a certain value, there is a near horizontal part of the line with reduced slope, and the $n^*$ value of this stage is lower than that of pure sandstone 2.

Furthermore, although the model established by the experiment was only applied to tight sandstone reservoirs, the modeling process took into account the influence of complex pore structures, heterogeneity, and the additional conductivity of clay, making it equally applicable to shale and igneous reservoirs. Furthermore, for shaly sandstone reservoirs with high clay content in other study areas, the equivalent pure rock resistivity index $I^*$ proposed in this paper, which eliminates the influence of clay conductivity, also provides a valuable reference for more accurately assessing rock conductivity.

## 7. Conclusions

In this study, an enhanced saturation parameter method based on the joint inversion of NMR and resistivity data was developed, and the $T_2$–$I^*$ model was successfully applied to tight sandstone reservoirs, yielding robust outcomes. Furthermore, an effective workflow for interpreting tight sandstone reservoirs using the $T_2$–$I^*$ model was proposed. This method accurately derives dynamic Archie equation parameters while comprehensively addressing vertical reservoir heterogeneity. Hence, the approach offers practical utility in calculating groundwater saturation and assessing $CO_2$ sequestration capacity. Moreover, the study observed varying fractal dimensions of pore spaces in large–pore segment and medium–pore segment with increasing water saturation. The restricted diffusion in medium–pore segment and significant heterogeneity contributed to irregular changes in the fractal dimension of medium–pore segment. Fluid distribution patterns in medium–pore segment were notably distinct from those in large–pore segment. In future research phases, additional microscopic scales (such as digital rock cores combined with scanning electron small–pore segment) can be employed to further analyze fluid distribution inside rock pores and its influence on NMR $T_2$ spectra. This study enhances the accuracy of fluid distribution calculations in porous media by analyzing the conductive properties of formation water. The saturation of underground water is a critical factor influencing the efficiency of $CO_2$ injection and its storage capacity. The findings provide a solid theoretical foundation for assessing $CO_2$ sequestration potential in engineering geology and predicting water saturation in porous media, while significantly improving the precision of quantitative evaluations of groundwater resources.

## CRediT authorship contribution statement

**Peng-Ji Zhang:** Writing – review & editing, Writing – original draft, Supervision, Software, Project administration, Methodology, Formal analysis, Data curation, Conceptualization. **Bao-Zhi Pan:** Writing – review & editing, Software, Project administration, Methodology, Investigation. **Yu-Hang Guo:** Writing – review & editing, Writing – original draft, Visualization, Supervision, Software, Methodology, Investigation, Funding acquisition, Data curation, Conceptualization. **Li-Hua Zhang:** Software, Methodology, Investigation. **Zhao-Wei Si:** Project administration, Methodology, Investigation, Data curation. **Feng Xu:** Project administration, Methodology, Investigation, Data curation. **Ming-Yue Zhu:** Software, Formal analysis. **Yan Li:** Visualization, Software.

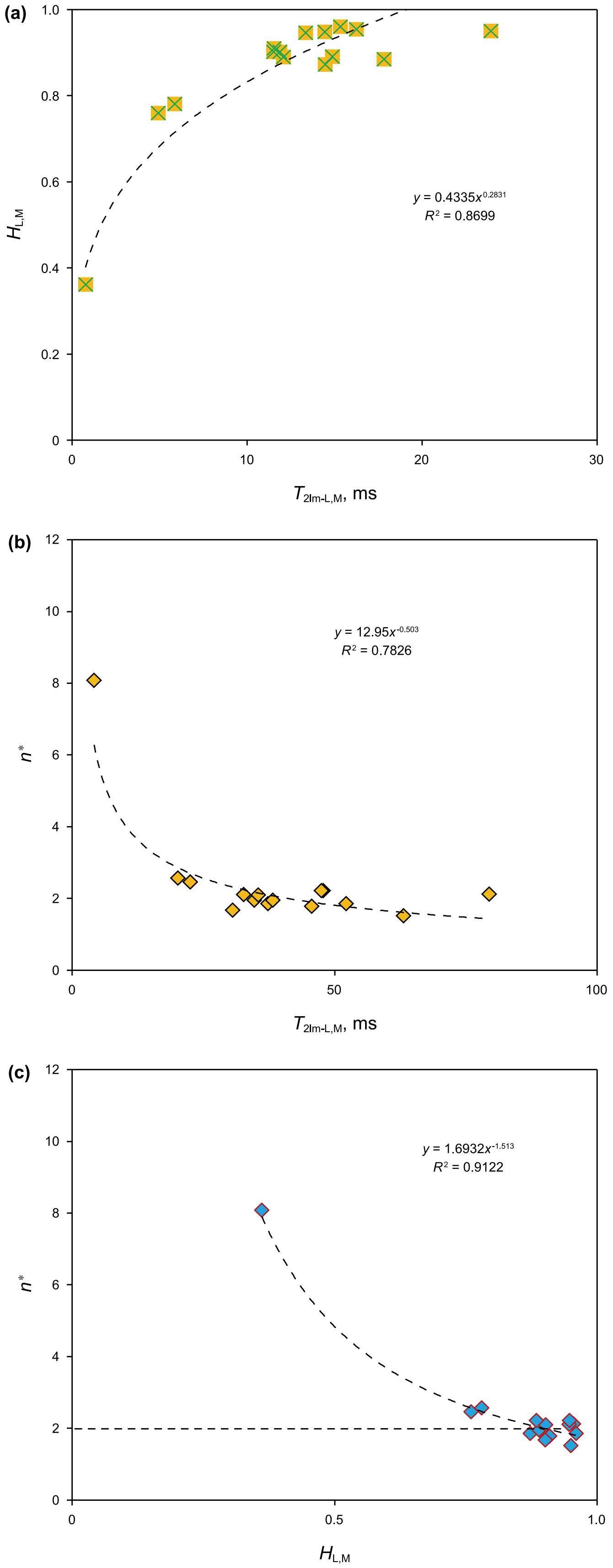

**Fig. 9.** Study on fluid distribution and conductivity in rock pore space: **(a)** intersection of $T_{2\mathrm{lm\text{-}L,M}}$ and $H_{\mathrm{L,M}}$; **(b)** intersection of $T_{2\mathrm{lm\text{-}L,M}}$ and $n^*$; **(c)** intersection of $H_{\mathrm{L,M}}$ and $n^*$.

## Data availability

The authors do not have permission to share.

## Declaration of competing interest

The authors declare that they have no known competing financial interests or personal relationships that could have appeared to influence the work reported in this paper.

## Acknowledgments

This work was supported in part by the Key National Research Project of China under Grant 2023YFC3707900; in part by the National Natural Science Foundation of China under Grant 42204122 and Grant 42072323.

## APPENDIX

$P_c$ and $T_2$ are both related to the pore structure of rocks, thus there is a certain relationship between them. The methods for converting $T_2$ distribution into capillary pressure curves mainly include the linear method and power function method. The linear method assumes that there is a linear relationship between $P_c$ and the reciprocal of $T_2$:

$$P_c = \frac{2\sigma\cos\theta}{r} = \frac{C_1}{C_2} \tag{A.1}$$

where $\sigma$ is the interfacial tension, $\mathrm{N\cdot m^{-1}}$; $\theta$ is the wetting contact angle, °; and $r$ is the capillary radius, μm. $C_1$ is a linear conversion coefficient and can be obtained through core data analysis.

At present, the power function method is widely used. Proposed the relationship between $T_2$ and the corresponding capillary radius (Guo et al., 2018):

$$T_2 = m_t \times r^{n_t} \tag{A.2}$$

where $m_t$ and $n_t$ are empirical coefficients, and can be obtained by analyzing the core data. According to previous research, rocks with low permeability and complex pore structure have a power function relationship between their transverse relaxation time and capillary radius (Pan et al., 2018). A power function relationship is adopted in this paper.

The Archie equation provides the relationship between resistivity index ($I$) and water saturation:

$$I = \frac{b}{S_w^n} = \frac{R_t}{R_0} \tag{A.3}$$

where $I$ is the resistivity index; $b$ is a parameter of the Archie equation; $n$ is the saturation index; $R_t$ is the sample resistivity; $R_0$ is the rock resistivity at 100% water saturation; and $S_w$ is the water saturation. This study is based on the fact that $I$ and $S_w$ curves are of a single fractal dimension, and the values of $b$ and $n$ are constant throughout the saturation distribution.

The capillary pressure can be expressed as follows:

$$P_c = P_{nw} - P_w = \frac{2\sigma\cos\theta}{r} \tag{A.4}$$

where $P_{nw}$ and $P_w$ are the pressures of non-wetting phase and wetting phase fluids, MPa. It is clear that the capillary pressure is inversely proportional to the capillary radius. The relationship between capillary pressure and saturation can be established through mercury intrusion experiments.

Toledo held that $P_c$ is a function of saturation, and the relation satisfies fractal theory (Toledo et al., 1994):

$$S_w \propto (P_c)^{-(3-D_f)} \tag{A.5}$$

where $D_f$ is the fractal dimension of pore size distribution. Li provided the relationship between capillary pressure and resistivity index based on the fractal model in porous media (Li and Williams, 2007):

$$P_{CD} = I^{\beta} = \frac{P_c}{P_e} \tag{A.6}$$

where $\beta$ is an index related to the thickness of the water film; $P_{CD}$ is the dimensionless capillary pressure; and $P_e$ is the threshold pressure, MPa.

The relationship between $T_2$ and $I$ is mainly studied based on fractal theory, and the expression of pore volume distribution in a given space is as follows:

$$V \propto r^{3-D_f} \tag{A.7}$$

where $V$ is the pore volume with a radius of $r$ in the rock sample, $\mu m^3$.

We then take the derivative of $r$ in Eq. (7):

$$\frac{dV}{dr} \propto r^{2-D_f} \tag{A.8}$$

According to the principle of fractal geometry, the expression for the cumulative pore volume $V_r$ with a pore size smaller than $r$ is obtained by integrating Eq. (8):

$$V_r = \int_{r_{\min}}^{r} a_v r^{2-D_f} dr = b_v \left( r^{3-D_f} - r_{\min}{}^{3-D_f} \right) \tag{A.9}$$

where $r_{\min}$ is the minimum pore radius of the reservoir rock, μm; $a_v$ is a proportional constant; and $b_v = \frac{a_v}{3-D_f}$.

The total pore volume $V$ of the reservoir:

$$V = b\left( r_{\max}^{3-D_f} - r_{\min}^{3-D_f} \right) \tag{A.10}$$

where $r_{\max}$ is the maximum pore radius of the reservoir rock, μm.

Though Eqs. (A.9) and (A.10), the expression for the cumulative volume fraction $S_r$ of pores with a pore size smaller than $r$ can be obtained:

$$S_r = \frac{V_r}{V} = \frac{r^{3-D_f} - r_{\min}^{3-D_f}}{r_{\max}^{3-D_f} - r_{\min}^{3-D_f}} \tag{A.11}$$

Considering $r_{\min} \ll r_{\max}$, Eq. (A.11) can be simplified as follows:

$$S_r = \left( \frac{r}{r_{\max}} \right)^{3-D_f} \tag{A.12}$$

In petrophysics, $S_r$ is the wetting phase saturation $S_w$. According to the BT model proposed by Brownstein and Tarr (1979), the relaxation behavior of fluids in porous media is influenced by free, surface and diffusion relaxation. The nuclear magnetic relaxation characteristics of hydrogen nuclei in core pore fluids are affected by slow relaxation in free pore fluids and fast relaxation near pore surfaces. Based on the cylindrical capillary model, many studies have held that transverse relaxation time and radius have a linear relationship. However, when the pore structure is complex, there is a power function relationship between transverse relaxation time and radius, See Eq. (2).

The expression for the geometric mean $T_{2\mathrm{lm}}$ is as follows:

$$\lg T_{2\mathrm{lm}} = \frac{\sum f_j \lg T_j}{\sum f_j} \tag{A.13}$$

where $T_j$ is the corresponding relaxation time; and $f_j$ is the porosity component of the corresponding relaxation time $T_j$ distribution.

We then substitute Eq. (2) into Eq. (12):

$$S_{\mathrm{w}} = S_r = \left(\frac{T_2}{T_{2\ \mathrm{max}}}\right)^{\frac{\left(3-D_{\mathrm{fT}}\right)}{n_{\mathrm{t}}}} = (T_{2\mathrm{D}})^{\frac{\left(3-D_{\mathrm{fT}}\right)}{n_{\mathrm{t}}}} \tag{A.14}$$

where $T_{2\mathrm{max}}$ is the maximum transverse relaxation time, corresponding to $r_{\mathrm{max}}$; and $T_{2\mathrm{D}}$ is the dimensionless transverse relaxation time, $T_{2\mathrm{D}}=T_2/T_{2\mathrm{max}}$. The relationship between $T_2$ distribution and wetting phase saturation is thus obtained. The transverse relaxation time and resistivity index, both functions of wetting phase saturation, are the basis for establishing the relationship in this paper.

Next, by substituting Eq. (A.3) into Eq. (A.14), the following relationship is obtained:

$$T_{2\mathrm{D}} = b\frac{n_{\mathrm{t}}}{n\left(3-D_{\mathrm{f}}\right)}(I)^{\frac{-n_{\mathrm{t}}}{n\left(3-D_{\mathrm{f}}\right)}} = b_{\mathrm{t}}(I)^{-\alpha} \tag{A.15}$$

Unlike the original formulation by Archie, the new analytical electrical conductivity expression has a direct physicogeometrical basis (Wei et al., 2015). We find

$$a = \frac{D_{\mathrm{fT}}}{\left(D_{\mathrm{fT}} + D_{\mathrm{T}} - 1\right)} \tag{A.16}$$

$$m = 1 + (D_{\mathrm{T}} - 1)\left(D_{\mathrm{E}} - D_{\mathrm{fT}}\right) \tag{A.17}$$

where $a$ is lithological coefficient; $m$ is Cementation exponent; $D_{\mathrm{E}}$ is the dimension in Euclidean space ($D_{\mathrm{E}} = 2$ or 3 in two−dimensional or three−dimensional space); and $D_{\mathrm{fT}}$ and $D_{\mathrm{T}}$ are the fractal dimensions of porous media pores and pore tortuosity, respectively, with the latter representing the degree of folding of current or fluid flow length. When $1 \le D_{\mathrm{T}} < 2$ or $1 \le D_{\mathrm{T}} < 3$, this respectively signifies two−or three−dimensional space. When $D_{\mathrm{T}} = 1$, it indicates that the pore is a straight channel. When $D_{\mathrm{T}}$ approaches 3, this indicates that the pore channel is very tortuous and fills the entire Euclidean space.

$D_{\mathrm{fT}}$ and $D_{\mathrm{T}}$ can be obtained from NMR data using the following equation:

$$D_{\mathrm{fT}} = D_{\mathrm{E}} - \frac{\ln \varphi}{\ln\left(\lambda_{\mathrm{min}}/\lambda_{\mathrm{max}}\right)} \tag{A.18}$$

$$D_{\mathrm{T}} = \left(D_{\mathrm{E}} - D_{\mathrm{fT}} + 1\right) + \frac{\left(D_{\mathrm{E}} - D_{\mathrm{fT}}\right)\ln\left[D_{\mathrm{fT}}/\left(D_{\mathrm{fT}} - 1\right)\right]}{\ln \varphi} \tag{A.19}$$

where $\lambda_{\mathrm{min}}$ and $\lambda_{\mathrm{max}}$ are the minimum and maximum pore sizes, respectively.

## References

Abidoye, L.K., Das, D.B., 2020. Impacts of dynamic capillary pressure effects in supercritical $CO_2$-water flow: experiments and numerical simulations. Adv. Water Resour. 136, 103504. https://doi.org/10.1016/j.advwatres.2020.103504.

Anand, V., Ali, M., 2015. New generation NMR tool for robust, continuous $T_1$ and $T_2$ measurements. In: 2016 SPWLA Annual Conference.

Archie, G.E., 1942. The electrical resistivity log as an aid in determining some reservoir characteristics. Trans. AIME 146, 54–62. https://doi.org/10.2118/942054-G.

Bachu, S., Adams, J.J., 2003. Sequestration of $CO_2$ in geological media in response to climate change: capacity of deep saline aquifers to sequester $CO_2$ in solution. Energy Convers. Manag. 44 (20), 3151–3175. https://doi.org/10.1016/S0196-8904(03)00101-8.

Bai, G.G., Sun, Q., Geng, J.S., et al., 2022. Resistivity of granite and sandstone varies with frequency and water saturation. Geomech. Geophys. Geo-Energy Geo-Resour. 8 (6), 198. https://doi.org/10.1007/s40948-022-00503-1.

Barros, C., Andrade, A., 2013. Determination of water saturation by angular competitive neural network. J. Pet. Sci. Eng. 102, 47–56. https://doi.org/10.1016/j.petrol.2013.01.007.

Brownstein, K.R., Tarr, C.E., 1979. Importance of classical diffusion in NMR studies of water in biological cells. Phys. Rev. Appl. 19 (6), 2446. https://doi.org/10.1103/PhysRevA.19.2446.

Byeungju, M., Sondergeld, C.H., Rai, C.S., 2019. Investigation of high frequency 1D NMR to characterize reservoir rocks. J. Pet. Sci. Eng. 176, 653–660. https://doi.org/10.1016/j.petrol.2019.01.093.

Cheng, H., Wang, F.G., Li, S.W., et al., 2024. The roles of microstructure and water mobility in pre-Darcy flow formation in saturated clay soil. J. Hydrol. 631, 130826. https://doi.org/10.1016/j.jhydrol.2024.130826.

Clavier, C., Coates, G., Dumanoir, J., 1984. Theoretical and experimental bases for the dual-water model for interpretation of shaly sands. SPE J. 24 (2), 153–168. https://doi.org/10.2118/6859-PA.

Coates, G.R., Xiao, L., Prammer, M.G., 1999. NMR Logging Principles and Applications. Halliburton Energy Services.

Duan, S.L., Li, B.B., Gao, Z., et al., 2023. Fractal apparent permeability model for coal under the coupling actions of stress and water. Energy Fuel. 37 (7), 4996–5012.

Feng, C., Han, C., Duan, W.H., et al., 2020a. Estimation of the resistivity index via nuclear magnetic resonance log data based on fractal theory. Geofluids 2020 (5), 1–10. https://doi.org/10.1155/2020/8871096.

Feng, C., Yang, Z., Feng, Z., et al., 2020b. A novel method to estimate resistivity index of tight sandstone reservoirs using nuclear magnetic resonance logs. J. Nat. Gas Sci. Eng. 79 (11), 103358. https://doi.org/10.1016/j.jngse.2020.103358.

Ge, X., Mao, G.D., Hu, S., et al., 2023. Laboratory NMR study to quantify the water saturation of partially saturated porous rocks. Lithosphere 2023 (1), 1214083. https://doi.org/10.2113/2023/1214083.

Guo, J.F., Xie, R.H., Zou, Y.L., et al., 2016. Simulation of NMR responses in sandstone and restricted diffusion. Chin. J. Geophys. 59 (7), 2703–2712. https://doi.org/10.6038/cjg20160733 (in Chinese).

Guo, Y.H., Pan, B.Z., Liu, W.B., 2016. A research on the relationship between resistivity index and relative permeability at different measurement conditions based on the pore structure. Environ. Fluid Mech. 16 (6), 1129–1141. https://doi.org/10.1007/s10652-016-9469-9.

Guo, Y.H., Pan, B.Z., Zhang, L.H., et al., 2018. Research and application of the relationship between transverse relaxation time and resistivity index in tight sandstone reservoir. J. Pet. Sci. Eng. 160, 597–604. https://doi.org/10.1016/j.petrol.2017.01.034.

Guo, Y.H., Pan, B.Z., Zhang, L.H., et al., 2022. A study on water saturation predictions in igneous reservoirs based on the relationship between the transverse relaxation time and the resistivity index. J. Pet. Sci. Eng. 208, 109519. https://doi.org/10.1016/j.petrol.2021.109519.

Haggerty, R., Sun, J.X., Yu, H.F., et al., 2023. Application of machine learning in groundwater quality modeling-A comprehensive review. Water Res. 233, 119745. https://doi.org/10.1016/j.watres.2023.119745.

Han, T.C., Yan, H., Fu, L.Y., 2021. A quantitative interpretation of the saturation exponent in archie's equations. Pet. Sci. 18 (2), 444–449. https://doi.org/10.1007/s12182-021-00547-0.

Heidary, M., 2021. A novel computational method for determination of water saturation in oil reservoirs using discrete wavelet transform and nuclear magnetic resonance (NMR) $T_2$ log. J. Pet. Sci. Eng. 205, 108828. https://doi.org/10.1016/j.petrol.2021.108828.

Huang, Z.Q., Zhou, X., Wang, H., et al., 2024. Stress sensitivity analysis of vuggy porous media based on two-scale fractal theory. Sci. Rep. 14 (1), 20710. https://doi.org/10.1038/s41598-024-71171-2.

Jackson, J.A., 1984. Nuclear magnetic resonance well logging. Log. Anal. 25 (5), 16–30.

Jongwon, J., Hu, J.W., 2016. Corrigendum to "impact of pressure and brine salinity on capillary pressure-water saturation relations in geological $CO_2$ sequestration". Adv. Condens. Matter Phys. 2016 (1), 1–11. https://doi.org/10.1155/2017/5367087.

Katz, A.J., Thompson, A.H., 1985. Fractal sandstone pores: implications for conductivity and pore formation. Phys. Rev. Lett. 54 (13), 1325–1328. https://doi.org/10.1103/PhysRevLett.54.1325.

Kim, S., Lee, K., Lee, M., et al., 2022. Evaluation of saturation changes during gas hydrate dissociation core experiment using deep learning with data augmentation. J. Pet. Sci. Eng. 209, 109820. https://doi.org/10.1016/j.petrol.2021.109820.

Korb, J.P., 2018. Multiscale nuclear magnetic relaxation dispersion of complex liquids in bulk and confinement. Prog. Nucl. Magn. Reson. Spectrosc. 104, 12–55. https://doi.org/10.1016/j.pnmrs.2017.11.001.

Kyeongmo, Koo, Hyunki, Kim, 2023. Stochastic estimation of hydraulic conductivity using self-organizing map. In: Geo-Risk 2023: Innovation in Data and Analysis Methods. https://doi.org/10.1061/9780784484975.025.

Li, K.W., Williams, W., 2007. Determination of Capillary Pressure Function from Resistivity Data. Transp. Porous Media. 67 (1), 1–15. https://doi.org/10.1007/s11242-006-0009-9.

Liu, C.W., Li, K.W., Ma, D., et al., 2016. More general relationship between capillary pressure and resistivity data in gas-water system. J. Pet. Sci. Eng. 146, 505–514. https://doi.org/10.1016/j.petrol.2016.07.008.

Liu, Y., Zhang, G., Qin, Y.Y., et al., 2023. Effects of magnetic field intensity and gradient on measurement results of core nuclear magnetic resonance $T_2$, spectrum. Pet. Geol. Exp. 45 (2), 378–384. https://doi.org/10.11781/sysydz202302378 (in Chinese).

Liu, H.Q., Xie, H.P., Wu, F., et al., 2024. A novel box-counting method for quantitative fractal analysis of three-dimensional pore characteristics in sandstone. Int. J. Min. Sci. Technol. 34 (4), 479–489. https://doi.org/10.1016/j.ijmst.2024.04.006.

Luo, A., Li, Y.M., Chen, X., et al., 2022. Review of $CO_2$ sequestration mechanism in saline aquifers. Nat. Gas. Ind. B. 9 (4), 383–393. https://doi.org/10.1016/j.ngib.2022.07.002.

Michael, J., Dick, M.J., Veselinovic, D., et al., 2022. NMR-based wettability index for unconventional rocks. Petrophysics 63 (3), 418–441. https://doi.org/10.30632/PJV63N3-2022a9.

Michelle, H.E., Martin, C.S., Timothy, A.M., et al., 2010. An anisotropic model for the electrical resistivity of two-phase geologic materials. Geophysics 75 (6), E161–E170. https://doi.org/10.30632/PJV63N3-2022a9.

Ming, F., Li, D.Q., Chen, L., 2020. Electrical resistivity of freezing clay: experimental study and theoretical model. J. Geophys. Res. Earth Surf. 125 (2), e2019JF005267. https://doi.org/10.1029/2019JF005267.

Mo, X.W., He, D.H., Li, Z.B., et al., 2001. The application of three–water conduction model in the interpretation of low–resistivity reservoir. Journal of Changchun University of Science and Technology 31 (1), 92–95. https://doi.org/10.13278/j.cnki.jjuese.2001.01.019 (in Chinese).

Pan, B.Z., Fang, C.H., Guo, Y.H., et al., 2018. Logging evaluation and productivity prediction of Sulige tight sandstone reservoirsbased on petrophysics transformation models. Chin. J. Geophys. 6l (12), 5115–5124. https://doi.org/10.6038/cjg2018L0724 (in Chinese).

Poupon, A., Leveaux, J., 1971. Evaluation of water saturation in shaly formations. Log. Anal. 12 (4), 3–8.

Qin, Y.Y., Zhang, G., Zhang, J.W., et al., 2021. Study on the influence of magnetic field intensity on $T_2$-$T_1$ two-dimensional nuclear magnetic resonance experiment. Prog. Geophys. 36 (5), 2082–2089. https://doi.org/10.6038/pg2021FF0244 (in Chinese).

Qiu, S.X., Yang, M., Xu, P., et al., 2020. A new fractal model for porous media based on low-field nuclear magnetic resonance. J. Hydrol. 586, 124890. https://doi.org/10.1016/j.jhydrol.2020.124890.

Simandoux, P., 1963. Dielectric measurements on porousmedia, application to the measurements of water satu-ration: study of behavior of argillaceous formations. Rev. Inst. Fr. Petrol 18 (Sl), 193–215.

Song, Z.Z., Lv, M.Y., Zhao, L.B., et al., 2024. A novel bound water occurrence model for tight sandstone. Fuel 357, 130030. https://doi.org/10.1016/j.fuel.2023.130030.

Toledo, P.G., Novy, R.A., Davis, H.T., et al., 1994. Capillary pressure, water relative permeability, electrical conductivity and capillary dispersion coefficient of fractal porous media at low wetting phase saturations. SPE Adv. Technol. 2 (1), 489–490. https://doi.org/10.2118/23675-PA.

Viaroli, S., Lancia, M., Re, V., 2022. Microplastics contamination of groundwater: current evidence and future perspectives. A review. Sci. Total Environ. 824, 153851. https://doi.org/10.1016/j.scitotenv.2022.153851.

Wang, D., Wei, F., Chen, X., et al., 2016. Application of modified Simandoux model in saturation logging interpretation. Offshore Oil 36 (3), 70–75. https://doi.org/10.3969/j.issn.1008-2336.2016.03.070 (in Chinese).

Wang, J.Q., Yuan, Y., Chen, J.W., et al., 2023. Geological conditions and suitability evaluation for $CO_2$ geological storage in deep saline aquifers of the Beibu Gulf Basin (South China). Energies 16 (5), 2360. https://doi.org/10.3390/en16052360.

Wasantha, P.L.P., Ranjit, P.G., Permata, G., et al., 2018. Damage evolution and deformation behaviour of dry and saturated sandstones: insights gleaned from optical measurements. Measurement 130, 8–17. https://doi.org/10.1016/j.measurement.2018.07.075.

Waxman, M.H., Smits, L.J.M., 1968. Electrical conductivities in oil-bearing shaly sands. SPE J. 8 (2), 107–122. https://doi.org/10.2118/1863-A.

Wei, W., Cai, J.C., Hu, X.Y., 2015. An electrical conductivity model for fractal porous media. Geophys. Res. Lett. 42 (12), 4833–4840. https://doi.org/10.1002/2015GL064460.

Xiao, L., Shi, Y.J., Li, G.R., et al., 2021. A method to predict the resistivity index for tight sandstone reservoirs from nuclear magnetic resonance data. AAPG (Am. Assoc. Pet. Geol.) Bull. 105 (5), 1009–1032. https://doi.org/10.1306/05222018269.

Xie, Z., Xiao, L.Z., Luo, S.H., et al., 2023. Numerical simulation study on the effect of temperature on the restricted diffusion in porous media. Magn. Reson. Lett 3 (2), 118–126. https://doi.org/10.1016/j.mrl.2023.03.007.

Xu, Z.P., Lin, M., Jiang, W.B., et al., 2023. Pore-morphology-based pore structure characterization for various porous media. Chem. Eng. Sci. 280, 118982. https://doi.org/10.1016/j.ces.2023.118982.

Xu, Y., Lin, S.H., Jiang, L.Y., et al., 2024. Dynamic mechanical characteristics of an artificial porous granite under various water saturation levels. Bull. Eng. Geol. Environ. 83 (1), 1–15. https://doi.org/10.1007/s10064-023-03483-y.

Zhang, Z.Z., Gao, F., 2015. Experimental investigation on the energy evolution of dry and water-saturated red sandstones. Int. J. Min. Sci. Technol. 25 (3), 383–388. https://doi.org/10.1016/j.ijmst.2015.03.009.

Zhang, L.H., Pan, B.Z., Li, Z.B., et al., 2010. New three-water conduction model and its application in evaluation of low porosity and low permeability reservoir. Oil Geophys. Prospect. 45 (3), 431–435 (in Chinese).

Zhang, F., Zhang, Q., Gardner, R.P., et al., 2018. Quantitative monitoring of $CO_2$ sequestration using thermal neutron detection technique in heavy oil reservoirs. International Int. J. Greenhouse Gas Control 79, 154–164. https://doi.org/10.1016/j.ijggc.2018.10.003.

Zhao, X.M., Yang, B.B., Yuan, S.C., et al., 2022. Seepage–fractal model of embankment soil and its application. Fractal Fract 6 (277), 277. https://doi.org/10.3390/fractalfract6050277.

Zhong, Z., Sun, A.Y., Ren, B., et al., 2021. A deep-learning-based approach for reservoir production forecast under uncertainty. SPE J. 26 (3), 1–27. https://doi.org/10.2118/205000-PA.